

SuperGS: Super-Resolution 3D Gaussian Splatting via Latent Feature Field and Gradient-guided Splitting

Shiyun Xie, Zhiru Wang, Yinghao Zhu, Chengwei Pan

Beihang University
pancw@buaa.edu.cn

Abstract

Recently, 3D Gaussian Splatting (3DGS) has excelled in novel view synthesis with its real-time rendering capabilities and superior quality. However, it faces challenges for high-resolution novel view synthesis (HRNVS) due to the coarse nature of primitives derived from low-resolution input views. To address this issue, we propose Super-Resolution 3DGS (SuperGS), which is an expansion of 3DGS designed with a two-stage coarse-to-fine training framework, utilizing pre-trained low-resolution scene representation as an initialization for super-resolution optimization. Moreover, we introduce Multi-resolution Feature Gaussian Splatting (MFGS) to incorporate a latent feature field for flexible feature sampling and Gradient-guided Selective Splitting (GSS) for effective Gaussian upsampling. By integrating these strategies within the coarse-to-fine framework ensure both high fidelity and memory efficiency. Extensive experiments demonstrate that SuperGS surpasses state-of-the-art HRNVS methods on challenging real-world datasets using only low-resolution inputs.

1 Introduction

Novel view synthesis (NVS) is crucial for applications like AR/VR, autonomous navigation, and 3D content creation in the field of computer vision and graphics (Deng et al. 2022; Tonderski et al. 2024; Poole et al. 2022). Traditional methods using meshes and points often sacrifice quality for speed (Munkberg et al. 2022; Botsch et al. 2005; Yifan et al. 2019). Conversely, Neural Radiance Fields (NeRF) (Mildenhall et al. 2021; Müller et al. 2022; Fridovich-Keil et al. 2022; Barron et al. 2021) have enhanced these tasks by implicitly modeling scene geometry and radiance, though their intensive computation limits real-time use.

A promising approach is 3D Gaussian Splatting (3DGS) (Kerbl et al. 2023), which uses 3D Gaussian primitives and a differentiable rasterization process for real-time, high-quality rendering. This technique avoids extensive ray sampling and employs clone and split strategies to enhance spatial coverage and scene representation. However, when handling high-resolution novel view synthesis (HRNVS), the vanilla 3DGS experiences significant performance degradation. Unlike NeRF-style models, which can

sample the color and opacity of any point due to continuous implicit scene representation, 3DGS cannot directly upsample the Gaussian primitives. Due to the lower sampling frequency of low-resolution images, primitives optimized in low-resolution scenarios often appear too coarse for high-resolution rendering, resulting in a loss of detail and visible artifacts (Yu et al. 2024). Moreover, associating spherical harmonics (SH) parameters with each Gaussian consumes a significant amount of memory, limiting practical applications.

To tackle these challenges, we propose a two-stage coarse-to-fine framework, in which we first optimize the scene representation under low-resolution input views and use this as the initialization for subsequent super-resolution. In order to upsample Gaussian primitives using information learned from low-resolution scenes, we introduce the Multi-resolution Feature Gaussian Splatting (MFGS) approach in place of conventional 3DGS pipeline. This method leverages hash-based grids to construct a latent feature field, allowing us to derive new Gaussian features by providing positions and view directions, thus bypassing the need to learn from scratch. We then render a feature map and employ an image decoder to synthesize novel view images, serving as a neural compensation for the information loss caused by previous interpolations. Additionally, utilizing feature vectors generated on-the-fly to replace the SH parameters traditionally bound to each Gaussian primitive significantly reduces memory requirements, which is particularly useful when representing high-resolution scenes.

When depicting high-resolution scenes, the need for more detailed primitives becomes apparent. To achieve it, large Gaussian primitives from lower-resolution scenes can be subdivided to obtain more details. However, not all regions need such fine granularity, particularly in textureless areas. Therefore, a Gradient-guided Selective Splitting (GSS) strategy is designed to adaptively subdivide coarse primitives. In the absence of high-resolution data, we employ a 2D pre-trained super-resolution (SR) model to generate pseudo high-resolution input views as a prior. Leveraging this prior, we initially identify and split only those coarse primitives that satisfy specific gradient and scale criteria to smaller ones, referred to as fine Gaussians. Subsequently, we optimize the scene representation, which includes both coarse and fine Gaussian primitives, as well as the latent feature

field, using the pseudo high-resolution information. This selective refinement of coarse Gaussians has been proven in subsequent experiments to ensure that the final count of Gaussians closely aligns with the number achieved using high-resolution ground truth images for supervision. This demonstrates that the upsampling method can reasonably and effectively refine detail representations. Furthermore, we introduce cross-view consistency constraint to mitigate the discrepancies that might arise from using pseudo labels from different viewpoints as direct supervision.

In summary, we make the following contributions:

- We introduce SuperGS, a novel approach for super-resolution 3D scene representation. This method utilizes a two-stage coarse-to-fine framework, which offers an optimal initialization for super-resolution by leveraging insights from low-resolution scenes, ultimately enhancing performance significantly.
- We present the MFGS and GSS strategies. The former allows sampling of Gaussian features at any desired position through a latent feature field, while the latter adeptly upsamples primitives to render high-resolution scenes with consistent and detailed 3D representation. Integrating these two approaches, SuperGS efficiently performs super-resolution on depicted scenes without the necessity of learning from scratch, effectively navigating the challenges of explicit representation.
- Extensive experiments demonstrate that SuperGS surpasses state-of-the-art methods in both NVS and HRNVS tasks on challenging real-world datasets, while significantly reducing the memory demands associated with storing numerous Gaussians.

2 Related Work

2.1 Novel View Synthesis

Novel view synthesis (NVS) is a complex task in computer vision, aimed at generating new viewpoint images from a set of posed photos. Neural radiance fields (NeRF) (Mildenhall et al. 2021) have excelled in NVS, encoding scene details into a MLP for volume rendering. However, NeRF’s limitations in detail capture and efficiency led to the development of Mip-NeRF (Barron et al. 2021) and InstantNGP (Müller et al. 2022), which enhance both aspects. Subsequent research (Liu et al. 2020; Hedman et al. 2021; Lin et al. 2022) has focused on finding a balance between rendering quality and efficiency, a persistently challenging task.

The recent development of 3D Gaussian Splatting (3DGS) (Kerbl et al. 2023) offers a potential solution to overcome the limitations of NeRF. By converting scene point clouds into anisotropic Gaussian primitives following Structure from Motion (SFM), 3DGS uses these primitives for explicit scene representation and employs a differentiable rasterizer for real-time, high-quality rendering. Despite its advances, the high memory requirements of 3DGS limit its broader application. Numerous studies (Lee et al. 2024; Liu et al. 2024; Zhang et al. 2024; Sun et al. 2024) address these challenges primarily by reducing the number of Gaussian primitives and compressing their attribute representations. Notably, some anchor-based methods (Lu

et al. 2024; Ren et al. 2024) predict the attributes of neural Gaussians on-the-fly based on corresponding anchor points, effectively minimizing memory use while ensuring high-quality rendering.

2.2 3D Scene Super-Resolution

High-resolution novel view synthesis (HRNVS) aims to synthesize high-resolution novel views from low-resolution inputs. NeRF-SR (Wang et al. 2022) samples multiple rays per pixel, enhancing multi-view consistency at the sub-pixel level. However, its depth-guided refinement strategy necessitates a ground truth high-resolution image as input, which is often difficult to provide in many scenarios. The same challenge applies to RefSR-NeRF (Huang et al. 2023).

Recently, 3DGS has become popular for its high-quality rendering and real-time rendering speeds. GaussianSR (Hu et al. 2024) leverages off-the-shelf 2D diffusion priors and uses Score Dilatation Sampling (SDS) (Gou et al. 2021) to extract 3D information from 2D knowledge. SRGS (Feng et al. 2024), on the other hand, uses high-resolution inputs from SwinIR as pseudo labels and introduces sub-pixel constraints to ensure view consistency. However, the pseudo labels provided by 2D SR models are often too smooth, making it difficult to capture sufficient detail directly in training. Additionally, representing high-resolution scenes requires substantial memory to store numerous Gaussians and their attributes. Our method addresses these issues through a Gradient-guided Selective Splitting strategy that effectively refines pretrained coarse primitives into fine ones. Thanks to the construction of a latent feature field, the splitted Gaussians do not need to learn from scratch. Furthermore, our approach significantly reduces memory usage, expanding its applicability, especially in high-resolution scenarios.

3 Methodology

In this work, we introduce a Super-resolution 3D Gaussian Splatting method for high-resolution novel view synthesis (HRNVS) from low-resolution input views, featuring a two-stage coarse-to-fine training framework. Figure 1 provides an overview of our SuperGS pipeline. We utilize the pretrained low-resolution scene representation as the initialization for further super-resolution optimization. Our proposed SuperGS incorporates three main strategies: a) multi-resolution Gaussian Splatting, b) gradient-guided selective splitting, and c) cross-view consistency constraint. We provide a detailed introduction to each component.

3.1 Multi-resolution Feature Gaussian Splatting

Grid Latent Feature Field Unlike NeRF, which adeptly achieves a continuous representation of 3D scenes, the vanilla 3DGS faces challenges when directly upscaling scenes due to its explicit scene representation. To address this, we delve into the concept of encapsulating the scene within a latent feature field. The straightforward method of using MLPs to map the positions and view directions of Gaussians into this latent space encounters significant drawbacks. Specifically, shallow MLPs often fail to capture enough information from positional encodings, whereas

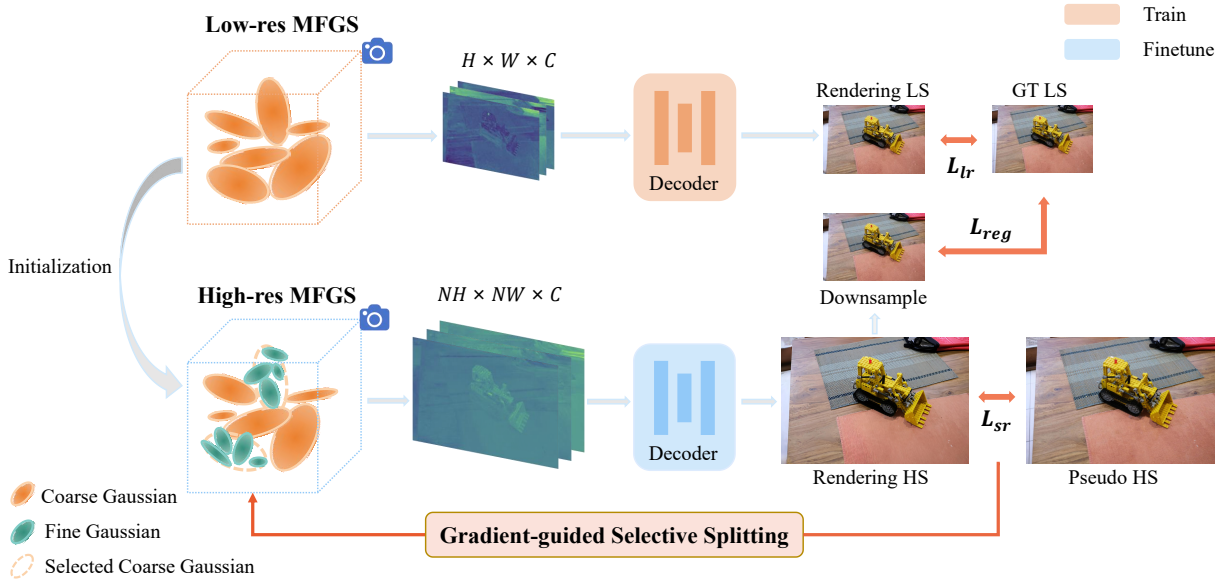


Figure 1: *Overview of our proposed SuperGS*. We replace the original 3DGS rendering pipeline with the Multi-resolution Feature Splatting (MFGS) approach by constructing a continuous latent feature field. To achieve super-resolution, we introduce a two-stage coarse-to-fine framework. Initially, we train a coarse MFGS model using low-resolution inputs. Subsequently, we implement a Gradient-guided Selective Splitting (GSS) strategy to refine coarse primitives into fine ones, effectively enhancing details under the guidance of a 2D prior. With further finetuning and consistency regularization, we develop a fine MFGS model that accurately represents high-resolution scenes.

deeper MLPs, despite their higher capacity, markedly increase computational costs and extend rendering times.

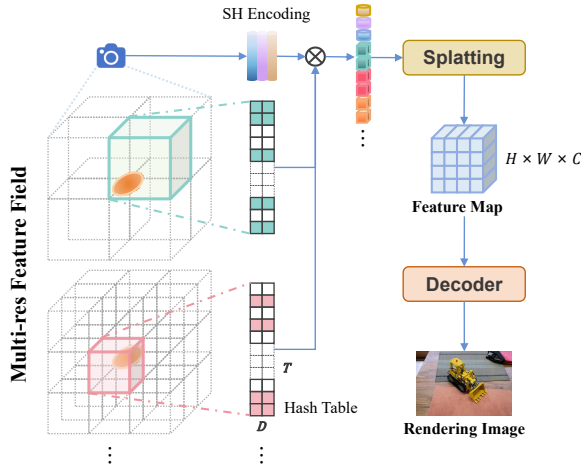


Figure 2: *Illustration of MFGS*. For a specific Gaussian, we identify its voxel across L resolution levels, extracting feature vectors of all voxel vertices from the corresponding hash table and deriving the l -th level feature via linear interpolation based on the Gaussian's center. We concatenate these features with SH encoding of direction, and an image decoder reconstructs the final image from this composite feature map, rendered through the differentiable rasterizer.

Drawing inspiration from InstantNGP (Müller et al. 2022), we adopt a similar strategy by storing view-

independent features in multi-resolution grids. This approach allows for efficient access to Gaussian features at arbitrary positions by indexing through hash tables followed by linear interpolation. As illustrated in Figure 2, for each Gaussian, we retrieve learnable feature vectors stored at grids with varying resolutions and perform linear interpolation to derive its feature representation. It is important to note that different levels of grids correspond to distinct hash tables. Specifically, there are L levels of grid resolutions, and the feature vector interpolated for the i -th Gaussian at the l -th level is denoted as f_i^l . From this, we construct its multi-resolution feature vector representation as follows:

$$f_{i,vi} = f_i^1 \otimes f_i^2 \otimes \dots \otimes f_i^L \quad (1)$$

where \otimes denotes the concatenation operation, and $f_{i,vi} \in \mathbb{R}^{L \times D}$ is referred to as a view-independent feature because it is exclusively related to the coordinates of the Gaussian, with D representing the feature dimension at each level. In the experiments, L and D are set to 16 and 2, respectively.

Similarly, to enable the grid feature field to extend to unbounded scenes, we reference the approach used in Mip-NeRF360 (Barron et al. 2021), which normalizes the coordinates of the Gaussians into a contracted space. The contraction is formally described as follows:

$$\text{contract}(p_i) = \begin{cases} p_i, & \|p_i\| \leq 1 \\ (2 - \frac{1}{\|p_i\|})(\frac{p_i}{\|p_i\|}), & \|p_i\| > 1 \end{cases} \quad (2)$$

where $p_i \in \mathbb{R}^3$ represents the position of i -th Gaussian.

Additionally, to account for view-dependent information, we encode the view directions using Spherical Harmonics

(SH) function, which is more suitable than component-wise frequency encoding. Subsequently, a tiny MLP (comprising two layers in practice) is used to map the concatenated feature vector and SH encodings to the final view-dependent feature. This process is formally expressed as follows:

$$f_i = \text{MLP}(f_{i-vi} \otimes \text{SH}(d_i)) \quad (3)$$

where $d_i \in \mathbb{R}^3$ denotes the view direction of the i -th Gaussian. It is noteworthy that, unlike binding SH parameters to each Gaussian, the same SH encoding and MLP parameters are used across the entire scene. Therefore, we just optimize a latent feature field that represents the entire scene instead of the SH parameters for each individual Gaussian.

Feature Gaussian Splatting and Image Decoder Firstly, a high-dimensional feature map is rendered, and then a post-decoder is used to obtain the final image. To render the feature map, we conduct a similar point-based α -blending approach. Given a camera pose v , we compute the feature $F_{v,p}$ of a pixel by blending a set of ordered Gaussians overlapping the pixel. The formula for $F_{v,p}$ is:

$$F_{v,p} = \sum_{i \in N} f_i a_i \prod_{j=1}^{i-1} (1 - a_j) \quad (4)$$

where α is derived by evaluating a 2D Gaussian and is further adjusted by a learned opacity specific to each Gaussian. In terms of the decoder, to strike a balance between speed and quality, we use a lightweight CNN-based architecture, primarily composed of a Bottleneck layer (He et al. 2016).

3.2 Gradient-guided Selective Splitting

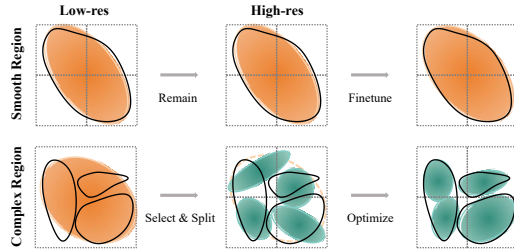


Figure 3: Illustration of GSS. Top row (Smooth Region): The coarse Gaussian effectively captures this area, so we retain it and apply finetuning at a low learning rate. Bottom row (Complex Region): The coarse Gaussian over-reconstructs this region, prompting us to split it into N_s fine ones to enhance details.

Observing that low-resolution primitives often appear too coarse for high-resolution rendering, and recognizing that high-resolution scenes require smaller Gaussians for detailed capture, we propose a Gradient-guided Selective Splitting (GSS) strategy shown in Figure 3. It selectively subdivides only those coarse primitives that inadequately represent their regions, while preserving larger coarse primitives in smoother, less detailed areas. Lacking high-resolution detail, we utilize a 2D pretrained SR model to generate high-resolution input views as pseudo-labels to guide this process.

Specifically, we consider those coarse Gaussians G_{coarse} , which are identified by their gradients and scales exceeding specific thresholds in complex regions. These are then subdivided into fine primitives, denoted as G_{fine} . Formally, we focus on the i -th Gaussian \mathcal{G}_i , which projects to the pixel-space point $\mu_i^k = (\mu_{i,x}^k, \mu_{i,y}^k)$ under viewpoint k , and its corresponding loss \mathcal{L}^k . The average view-space positional gradient is computed every 100 training iterations as follows:

$$\nabla_{\mu_i} \mathcal{L} = \frac{1}{M} \sum_{k=1}^M \sqrt{\left(\frac{\partial \mathcal{L}^k}{\partial \mu_{i,x}^k} \right)^2 + \left(\frac{\partial \mathcal{L}^k}{\partial \mu_{i,y}^k} \right)^2} \quad (5)$$

where M denotes the cumulative number of viewpoints in which Gaussian \mathcal{G}_i is engaged over 100 iterative cycles. The division of \mathcal{G}_i is enacted once specific criteria are satisfied:

$$\nabla_{\mu_i} \mathcal{L} > \tau_p \text{ and } \|S_i\| > \tau_s \quad (6)$$

where τ_p and τ_s represent the gradient threshold and scale threshold, respectively.

Algorithm 1: Gradient-guided selective splitting

Input: Feature Field \mathcal{F} , Splitting Number N_s , G_{coarse}

Output: \mathcal{F} , G_{coarse} , G_{fine}

```

1:  $G_{\text{fine}} \leftarrow \emptyset$ 
2: for  $i \leftarrow 0$  to Coarse2FineIteration do
3:    $\mathcal{L} \leftarrow \text{UpdateLoss}()$ 
4:   if IsSplitIteration( $i$ ) then
5:     for  $\mathcal{G}_j \in G_{\text{coarse}}$  do
6:       if  $\nabla_{\mu_j} \mathcal{L} > \tau_p$  and  $\|S_j\| > \tau_s$  then
7:          $G_{N_s}(p', \Sigma', \alpha', f') = \text{SplitCoarse}(p, \Sigma, \alpha, \mathcal{F})$ 
8:          $G_{\text{fine}} = G_{\text{fine}} \cup G_{N_s}$ 
9:          $G_{\text{coarse}} = G_{\text{coarse}} - \mathcal{G}_j$ 
10:      end if
11:    end for
12:  end if
13: end for
14: DensifyFine( $G_{\text{fine}}$ )
15: Finetune( $G_{\text{coarse}}$ ,  $\mathcal{F}$ )

```

The GSS procedure, detailed in Algorithm 1, involves splitting selected coarse primitives into N_s finer segments, where N_s is tied to the super-resolution ratio. These fine Gaussians are initialized using the coarse Gaussian as a sampling PDF and are scaled down to $1/(0.8 \times N_s)$. We optimize scene representation by implement the original densification scheme on the fine Gaussians, discarding those with low opacities, and enhancing the multi-resolution hash table, image decoder, and attributes of remaining coarse Gaussians using a reduced learning rate.

3.3 Cross-view Consistency Constraint

When training high-resolution scenes, we employ the overall loss function as SRGS (Feng et al. 2024):

$$\mathcal{L} = (1 - \lambda_{\text{reg}}) \mathcal{L}_{\text{hr}} + \lambda_{\text{reg}} \mathcal{L}_{\text{reg}} \quad (7)$$

where,

$$\begin{aligned} \mathcal{L}_{\text{hr}} = & (1 - \lambda_{\text{ssim}}) \mathcal{L}_1(I_{\text{hr}}^{\text{render}}, I_{\text{hr}}^{\text{pseudo}}) \\ & + \lambda_{\text{ssim}} \mathcal{L}_{D-\text{SSIM}}(I_{\text{hr}}^{\text{render}}, I_{\text{hr}}^{\text{pseudo}}) \end{aligned} \quad (8)$$

Table 1: Quantitative comparison for NVS ($\times 1$) on real-world datasets.

Dataset Method&Metric	Mip-NeRF360					Deep Blending					Tanks&Temples				
	PSNR	SSIM	LPIPS	FPS	Mem	PSNR	SSIM	LPIPS	FPS	Mem	PSNR	SSIM	LPIPS	FPS	Mem
3DGS	28.08	0.836	0.157	80	737	28.75	0.874	0.129	123	366	24.61	0.883	0.104	110	149
Scaffold-GS	29.33	0.873	0.111	108	163	29.69	0.897	0.107	187	48	25.67	0.897	0.092	125	50
Ours	29.44	0.865	0.130	47	123	29.88	0.898	0.109	70	99	26.35	0.900	0.099	98	67

$$\mathcal{L}_{reg} = (1 - \lambda_{ssim})\mathcal{L}_1(I_{lr}^{render}, I_{lr}^{gt}) + \lambda_{ssim}\mathcal{L}_{D-SSIM}(I_{lr}^{render}, I_{lr}^{gt}) \quad (9)$$

where I_{hr} is the high-resolution image rendered by the MFGS pipeline, while I_{lr} is obtained by downsampling I_{hr} through average pooling to match the resolution of the input viewpoint images. As we independently upscale each input viewpoint image using a 2D pretrained SR model, the high-resolution pseudo-labels for the same area across different viewpoints may contain inconsistencies. Therefore, we incorporate a sub-pixel constraint as a regularization term to further ensure cross-view consistency.

4 Experiments

4.1 Experimental Setups

Datasets and Metrics We conduct a comprehensive evaluation of our proposed model using PSNR, SSIM and LPIPS (Zhang et al. 2018) metrics. Our evaluation covers 13 scenes from real-world datasets, including 9 scenes from Mip-NeRF360 (Barron et al. 2022), 2 scenes from Deep Blending (Hedman et al. 2018) and 2 scenes from Tanks&Temples (Knapsch et al. 2017). For Mip-NeRF360, We downsample the training views by a factor of 8 as low-resolution inputs for the $\times 2$ and $\times 4$ HRNVS tasks. And for Deep Blending and Tanks&Temples, We downsample the training views by a factor of 4 as inputs. Notably, we proportionally resize images with excessively high resolution to a 1.6k resolution for the longer edge and select every eighth photo for testing, following 3DGS (Kerbl et al. 2023).

Baselines We conduct simultaneous comparisons between the same resolution NVS and the super-resolution HRNVS tasks with the latest state-of-the-art methods. For the NVS task, we benchmark our methods against 3DGS (Kerbl et al. 2023) and Scaffold-GS (Lu et al. 2024). To ensure a fair comparison, we execute the source codes of both methods at identical resolution settings. For the HRNVS task, our results compare with those from 3DGS, Scaffold-GS, GaussianSR (Hu et al. 2024), and SRGS (Feng et al. 2024). For 3DGS and Scaffold-GS, we train using low-resolution input views and directly render high-resolution images. Additionally, to maintain fairness in the comparisons, we utilize the same 2D pretrained SR model, SwinIR, to upscale the low-resolution images rendered by these methods, referred to as 3DGS-SwinIR and Scaffold-SwinIR. Regarding GaussianSR, which has not released its source code, we directly cite the results from its paper for comparison. For SRGS, we run the source code to obtain both qualitative and quantitative under identical conditions.

Implementation Details 3DGS-based methods are our primary baseline due to their excellent NVS quality and fast rendering. For fair comparison, we use SwinIR (Liang et al. 2021) as the 2D pretrained SR model, mirroring SRGS (Feng et al. 2024). We set gradient thresholds $\tau_p = 0.0002$ and $\tau_s = 0.01$. For HRNVS tasks, we set $N_s = 5$ for $\times 2$ scale and $N_s = 7$ for $\times 4$ scale. Loss weights λ_{reg} and λ_{ssim} are both set to 0.2. All our experiments are conducted on a single RTX 4090 GPU.

4.2 Quantitative Evaluation

Experiments on NVS We first compare the performance of novel view synthesis at the original resolution on real-world datasets, where both input and output share the same resolution size, to demonstrate the effectiveness of our proposed MFGS method. As shown in Table 1, compared to the latest 3DGS-based methods, our method exhibits significant advantages in PSNR and SSIM metrics and achieves comparable results in the LPIPS metric. Additionally, by eliminating the costly SH parameters bound to each Gaussian and instead storing a limited-length hash feature vector table, we significantly reduce memory usage compared to 3DGS, which is especially important in high-resolution scenarios. Furthermore, although the need for a post-image decoder to compensate for the loss of information in interpolated features slightly slows down rendering speeds, we still meet the requirements for real-time rendering.

Experiments on HRNVS Table 3 and Table 2 showcase quantitative comparison results for the $\times 2$ and $\times 4$ HRNVS tasks on the real-world datasets. Our proposed SuperGS nearly consistently and significantly outperforms previous state-of-the-art methods in terms of PSNR and SSIM. Additionally, our method reduces memory usage by $\times 2$ to $\times 4$ compared to the SRGS method, facilitating broader application in real-world scenarios. Notably, Scaffold-GS reports lower memory usage because it is only trained on low-resolution scenes. This underscores the effectiveness and practicality of our approach to HRNVS tasks.

4.3 Qualitative Evaluation

As illustrated in Figure 4, our method has significantly enhanced the visual effects in HRNVS tasks, such as rendering details and fidelity, across both indoor and outdoor scenes. In contrast, the Gaussian from low-resolution scenes is too coarse for high-resolution rendering, causing vanilla 3DGS (Kerbl et al. 2023) and Scaffold-GS (Lu et al. 2024) to exhibit severe artifacts. Applying SwinIR (Liang et al. 2021) directly to upsample low-resolution rendered images results

Table 2: Quantitative comparison for HRNVS ($\times 2$ and $\times 4$) on Mip-NeRF360 and Deep Blending datasets. Mip-NeRF360 is downsampled by a factor of 8, and Deep Blending by a factor of 4, for low-resolution inputs. Due to table size limitations, we only report the key PSNR and SSIM metrics, along with memory usage.

Dataset Method&Metric	Mip-NeRF360 $\times 2$			Mip-NeRF360 $\times 4$			Deep Blending $\times 2$			Deep Blending $\times 4$		
	PSNR	SSIM	Mem	PSNR	SSIM	Mem	PSNR	SSIM	Mem	PSNR	SSIM	Mem
3DGS	23.41	0.727	598	20.38	0.582	475	27.88	0.863	395	24.80	0.769	410
3DGS-SwinIR	24.77	0.708	662	23.47	0.605	539	27.56	0.846	459	25.65	0.789	474
Scaffold-GS	23.37	0.723	156	20.30	0.584	134	28.79	0.885	48	27.51	0.862	49
Scaffold-SwinIR	24.83	0.703	220	23.49	0.600	198	28.09	0.854	112	27.45	0.838	113
GaussianSR	-	-	-	25.60	0.663	-	-	-	-	28.28	0.873	-
SRGS	26.24	0.768	559	25.16	0.710	464	28.98	0.885	427	28.80	0.875	437
Ours	26.69	0.766	203	25.52	0.716	204	29.61	0.889	101	29.21	0.880	100

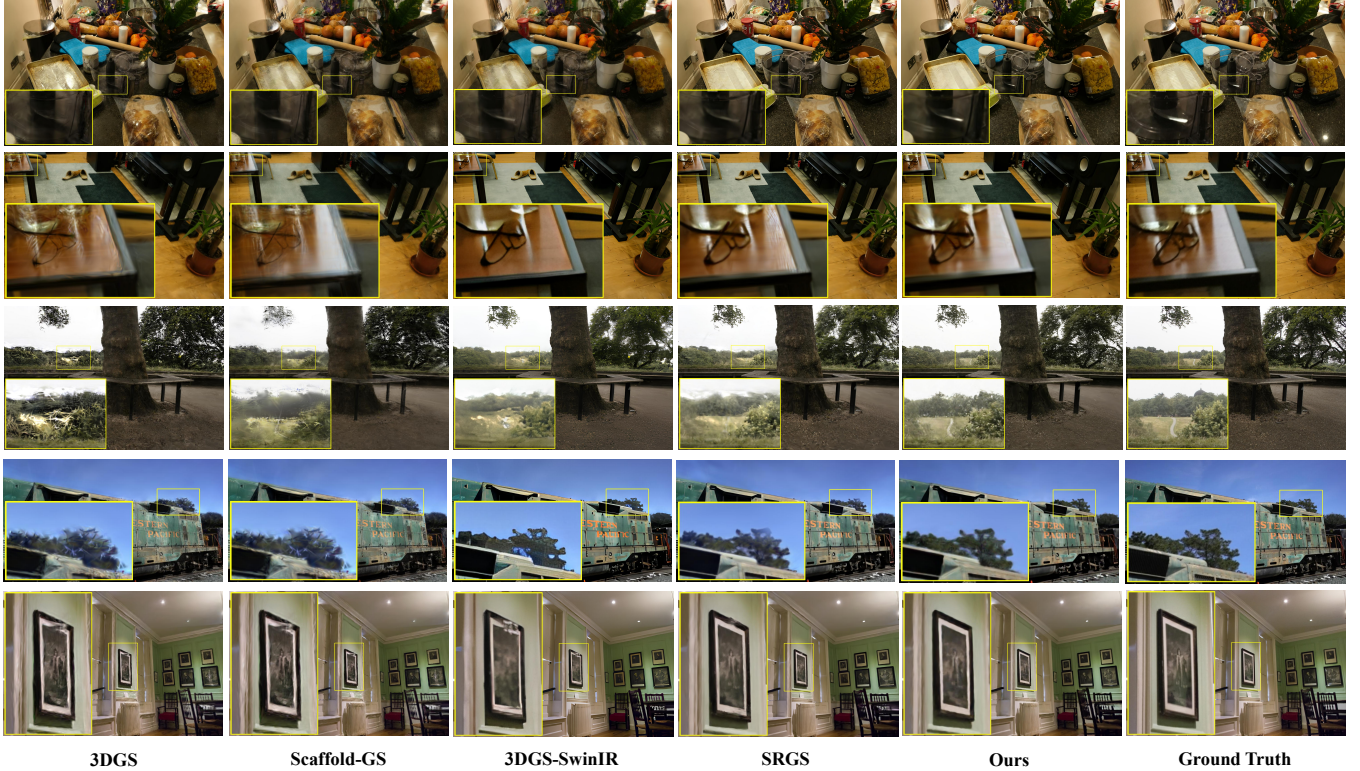


Figure 4: Qualitative comparison of the HRNVS ($\times 4$) on real-world datasets. We highlight the difference with colored patches.

Table 3: Quantitative comparison for HRNVS ($\times 2$ and $\times 4$) on the Tanks&Temples dataset. Tanks&Temples is downsampled by a factor of 4 to serve as low-resolution inputs.

Dataset Method&Metric	Tanks&Temples $\times 2$			Tanks&Temples $\times 4$		
	PSNR	SSIM	Mem	PSNR	SSIM	Mem
3DGS	20.78	0.768	152	17.87	0.621	156
3DGS-SwinIR	22.11	0.765	216	20.57	0.656	220
Scaffold-GS	20.90	0.781	50	17.74	0.629	51
Scaffold-SwinIR	22.47	0.773	114	20.82	0.660	115
SRGS	23.28	0.816	157	21.61	0.708	163
Ours	24.41	0.822	78	22.25	0.708	79

in insufficient detail, leading to overly smooth and unrealistic outcomes, and fails to ensure consistency across different viewpoints. Additionally, SRGS (Feng et al. 2024) still encounters issues with reconstruction errors and artifacts.

4.4 Ablation Studies

In Table 4, we conduct ablation experiments on the components proposed in SuperGS, individually demonstrating the effectiveness of our proposed Multi-resolution Feature Gaussian Splatting (MFGS), Gradient-guided Selective Splitting (GSS), and Cross-view Consistency Regularization.

Effectiveness of MFGS As shown in Table 4, we first compare the performance differences between using a pre

Table 4: *Ablation experiments for NVS ($\times 1$) and HRNVS ($\times 2$ and $\times 4$) on the counter scene from Mip-NeRF360 Dataset.* The full method contains MFGS, GSS and \mathcal{L}_{reg} .

Scene	counter $\times 1$			-		
	PSNR	SSIM	LPIPS	PSNR	SSIM	LPIPS
Pre-decoder	29.74	0.929	0.078	-	-	-
Post-decoder	30.68	0.936	0.074	-	-	-
counter $\times 2$			counter $\times 4$			
3DGS	25.66	0.834	0.179	23.21	0.750	0.364
MFGS	26.64	0.833	0.196	24.66	0.762	0.345
MFGS-SwinIR	27.30	0.825	0.185	26.37	0.790	0.289
MFGS-SRGS	27.76	0.862	0.182	27.01	0.827	0.296
MFGS-GSS	28.19	0.864	0.175	27.05	0.823	0.293
Full(Ours)	28.52	0.872	0.171	27.44	0.830	0.289

color decoder (named Pre-decoder) and a post image decoder (named Post-decoder) within the same resolution for NVS tasks. As the metrics and Figure 5 indicate, using Post-decoder can compensate for the information loss caused by interpolation in the grid feature field, as we anticipate.



Figure 5: *Ablation study on MFGS.* MFGS with Pre-decoder and MFGS with Post-decoder are compared.

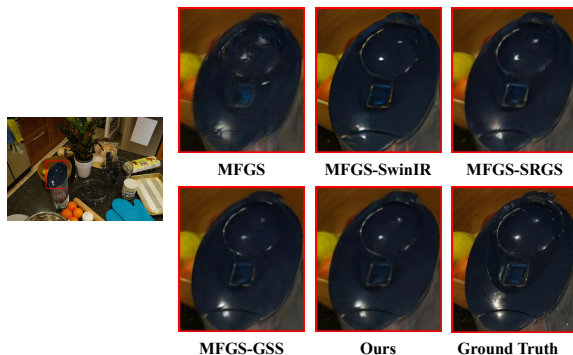


Figure 6: *Ablation study on GSS and \mathcal{L}_{reg} .* We evaluate various methods combined with MFGS model, demonstrating the effectiveness of GSS strategy and the cross-view consistency constraint.

Furthermore, without incorporating prior knowledge, specifically by not using pseudo-labels from a pre-trained 2D SR model and training solely on low-resolution input images, MFGS surpasses the performance of 3DGS, as shown in Table 4. Supplementary materials provide additional visual evidence supporting this conclusion.

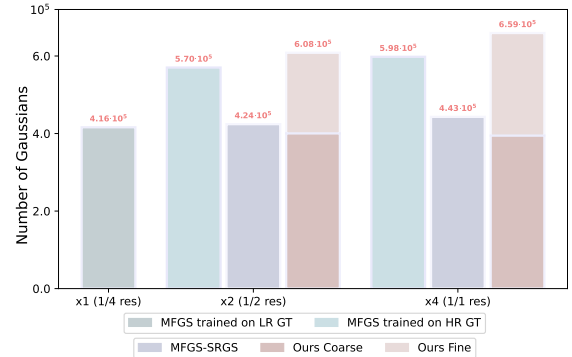


Figure 7: *Comparison of the final Gaussian count in the kitchen scene using MFGS-SRGS versus our method with low-resolution inputs.* Our approach closely matches the number of Gaussians from the MFGS model using high-resolution ground truth inputs, demonstrating the validity of the GSS strategy.

Effectiveness of GSS Based on the MFGS method, we further design experiments to demonstrate the effectiveness of the GSS strategy. Specifically, we test the super-resolution of low-resolution images obtained from MFGS using SwinIR (named MFGS-SwinIR), as well as the combination of MFGS with pseudo-label supervision and regularization constraints from SRGS (named MFGS-SRGS). Both the experimental results and Figure 6 illustrate the effectiveness of GSS. Additionally, we test the number of primitives used to represent the scene when combining MFGS with both GSS and SRGS methods. As shown in Figure 7, our method aligns well with the number of Gaussians used when training with high-resolution ground truth inputs. Using GSS allows for more accurate capture of detailed areas within the scene and implements a more rational scene representation upsampling strategy. Furthermore, integrating Cross-view Consistency regularization with MFGS-GSS can further improve the performance, avoiding the ambiguities caused by individually generating each 2D pseudo label.

5 Conclusion

In this paper, we introduce SuperGS, an expansion of 3DGS designed to synthesize high-resolution novel views from only low-resolution inputs. The method is founded on a two-stage coarse-to-fine framework, where pretrained low-resolution scene representation serves as the starting point for super-resolution optimization. Additionally, we replace the vanilla 3DGS pipeline with our Multi-resolution Feature Gaussian Splatting, and we incorporate Gradient-guided Selective Splitting to effectively enhance detail. Our experimental results showcase SuperGS’s outstanding performance in both novel view synthesis (NVS) and high-resolution novel view synthesis (HRNVS) tasks. Notably, we utilize the 2D super-resolution model SwinIR for a fair comparison with SRGS, but the framework is adaptable to incorporate any arbitrary-scale 2D super-resolution model, potentially enabling arbitrary-scale super-resolution achievements within this framework.

References

Agustsson, E.; and Timofte, R. 2017. NTIRE 2017 Challenge on Single Image Super-Resolution: Dataset and Study. In *The IEEE Conference on Computer Vision and Pattern Recognition (CVPR) Workshops*.

Barron, J. T.; Mildenhall, B.; Tancik, M.; Hedman, P.; Martin-Brualla, R.; and Srinivasan, P. P. 2021. Mip-nerf: A multiscale representation for anti-aliasing neural radiance fields. In *Proceedings of the IEEE/CVF international conference on computer vision*, 5855–5864.

Barron, J. T.; Mildenhall, B.; Verbin, D.; Srinivasan, P. P.; and Hedman, P. 2022. Mip-nerf 360: Unbounded anti-aliased neural radiance fields. In *Proceedings of the IEEE/CVF Conference on Computer Vision and Pattern Recognition*, 5470–5479.

Botsch, M.; Hornung, A.; Zwicker, M.; and Kobbelt, L. 2005. High-quality surface splatting on today’s GPUs. In *Proceedings Eurographics/IEEE VGTC Symposium Point-Based Graphics*, 2005., 17–141. IEEE.

Deng, N.; He, Z.; Ye, J.; Duinkharjav, B.; Chakravarthula, P.; Yang, X.; and Sun, Q. 2022. Fov-nerf: Foveated neural radiance fields for virtual reality. *IEEE Transactions on Visualization and Computer Graphics*, 28(11): 3854–3864.

Feng, X.; He, Y.; Wang, Y.; Yang, Y.; Kuang, Z.; Jun, Y.; Fan, J.; et al. 2024. SRGS: Super-Resolution 3D Gaussian Splatting. *arXiv preprint arXiv:2404.10318*.

Fridovich-Keil, S.; Yu, A.; Tancik, M.; Chen, Q.; Recht, B.; and Kanazawa, A. 2022. Plenoxels: Radiance fields without neural networks. In *Proceedings of the IEEE/CVF Conference on Computer Vision and Pattern Recognition*, 5501–5510.

Gou, J.; Yu, B.; Maybank, S. J.; and Tao, D. 2021. Knowledge distillation: A survey. *International Journal of Computer Vision*, 129(6): 1789–1819.

He, K.; Zhang, X.; Ren, S.; and Sun, J. 2016. Deep residual learning for image recognition. In *Proceedings of the IEEE conference on computer vision and pattern recognition*, 770–778.

Hedman, P.; Philip, J.; Price, T.; Frahm, J.-M.; Drettakis, G.; and Brostow, G. 2018. Deep blending for free-viewpoint image-based rendering. *ACM Transactions on Graphics (ToG)*, 37(6): 1–15.

Hedman, P.; Srinivasan, P. P.; Mildenhall, B.; Barron, J. T.; and Debevec, P. 2021. Baking neural radiance fields for real-time view synthesis. In *Proceedings of the IEEE/CVF international conference on computer vision*, 5875–5884.

Hu, J.; Xia, B.; Chen, B.; Yang, W.; and Zhang, L. 2024. GaussianSR: High Fidelity 2D Gaussian Splatting for Arbitrary-Scale Image Super-Resolution. *arXiv preprint arXiv:2407.18046*.

Huang, X.; Li, W.; Hu, J.; Chen, H.; and Wang, Y. 2023. Refsr-nerf: Towards high fidelity and super resolution view synthesis. In *Proceedings of the IEEE/CVF Conference on Computer Vision and Pattern Recognition*, 8244–8253.

Kerbl, B.; Kopanas, G.; Leimkühler, T.; and Drettakis, G. 2023. 3D Gaussian Splatting for Real-Time Radiance Field Rendering. *ACM Trans. Graph.*, 42(4): 139–1.

Knapitsch, A.; Park, J.; Zhou, Q.-Y.; and Koltun, V. 2017. Tanks and temples: Benchmarking large-scale scene reconstruction. *ACM Transactions on Graphics (ToG)*, 36(4): 1–13.

Lee, J. C.; Rho, D.; Sun, X.; Ko, J. H.; and Park, E. 2024. Compact 3d gaussian representation for radiance field. In *Proceedings of the IEEE/CVF Conference on Computer Vision and Pattern Recognition*, 21719–21728.

Liang, J.; Cao, J.; Sun, G.; Zhang, K.; Van Gool, L.; and Timofte, R. 2021. Swinir: Image restoration using swin transformer. In *Proceedings of the IEEE/CVF international conference on computer vision*, 1833–1844.

Lim, B.; Son, S.; Kim, H.; Nah, S.; and Lee, K. M. 2017. Enhanced Deep Residual Networks for Single Image Super-Resolution. In *The IEEE Conference on Computer Vision and Pattern Recognition (CVPR) Workshops*.

Lin, H.; Peng, S.; Xu, Z.; Yan, Y.; Shuai, Q.; Bao, H.; and Zhou, X. 2022. Efficient neural radiance fields for interactive free-viewpoint video. In *SIGGRAPH Asia 2022 Conference Papers*, 1–9.

Liu, L.; Gu, J.; Zaw Lin, K.; Chua, T.-S.; and Theobalt, C. 2020. Neural sparse voxel fields. *Advances in Neural Information Processing Systems*, 33: 15651–15663.

Liu, X.; Wu, X.; Zhang, P.; Wang, S.; Li, Z.; and Kwong, S. 2024. CompGS: Efficient 3D Scene Representation via Compressed Gaussian Splatting. *arXiv preprint arXiv:2404.09458*.

Lu, T.; Yu, M.; Xu, L.; Xiangli, Y.; Wang, L.; Lin, D.; and Dai, B. 2024. Scaffold-gs: Structured 3d gaussians for view-adaptive rendering. In *Proceedings of the IEEE/CVF Conference on Computer Vision and Pattern Recognition*, 20654–20664.

Mildenhall, B.; Srinivasan, P. P.; Tancik, M.; Barron, J. T.; Ramamoorthi, R.; and Ng, R. 2021. Nerf: Representing scenes as neural radiance fields for view synthesis. *Communications of the ACM*, 65(1): 99–106.

Müller, T.; Evans, A.; Schied, C.; and Keller, A. 2022. Instant neural graphics primitives with a multiresolution hash encoding. *ACM transactions on graphics (TOG)*, 41(4): 1–15.

Munkberg, J.; Hasselgren, J.; Shen, T.; Gao, J.; Chen, W.; Evans, A.; Müller, T.; and Fidler, S. 2022. Extracting triangular 3d models, materials, and lighting from images. In *Proceedings of the IEEE/CVF Conference on Computer Vision and Pattern Recognition*, 8280–8290.

Poole, B.; Jain, A.; Barron, J. T.; and Mildenhall, B. 2022. Dreamfusion: Text-to-3d using 2d diffusion. *arXiv preprint arXiv:2209.14988*.

Ren, K.; Jiang, L.; Lu, T.; Yu, M.; Xu, L.; Ni, Z.; and Dai, B. 2024. Octree-gs: Towards consistent real-time rendering with lod-structured 3d gaussians. *arXiv preprint arXiv:2403.17898*.

Sun, X.; Lee, J. C.; Rho, D.; Ko, J. H.; Ali, U.; and Park, E. 2024. F-3DGS: Factorized Coordinates and Representations for 3D Gaussian Splatting. *arXiv preprint arXiv:2405.17083*.

Tonderski, A.; Lindström, C.; Hess, G.; Ljungbergh, W.; Svensson, L.; and Petersson, C. 2024. Neurad: Neural rendering for autonomous driving. In *Proceedings of the IEEE/CVF Conference on Computer Vision and Pattern Recognition*, 14895–14904.

Wang, C.; Wu, X.; Guo, Y.-C.; Zhang, S.-H.; Tai, Y.-W.; and Hu, S.-M. 2022. Nerf-sr: High quality neural radiance fields using supersampling. In *Proceedings of the 30th ACM International Conference on Multimedia*, 6445–6454.

Wang, X.; Yu, K.; Dong, C.; and Loy, C. C. 2018. Recovering realistic texture in image super-resolution by deep spatial feature transform. In *The IEEE Conference on Computer Vision and Pattern Recognition (CVPR)*.

Yifan, W.; Serena, F.; Wu, S.; Öztireli, C.; and Sorkine-Hornung, O. 2019. Differentiable surface splatting for point-based geometry processing. *ACM Transactions on Graphics (TOG)*, 38(6): 1–14.

Yu, Z.; Chen, A.; Huang, B.; Sattler, T.; and Geiger, A. 2024. Mip-splatting: Alias-free 3d gaussian splatting. In *Proceedings of the IEEE/CVF Conference on Computer Vision and Pattern Recognition*, 19447–19456.

Zhang, F.; Zhang, T.; Zhang, L.; Huang, H.; and Luo, Y. 2024. Gaussian-Forest: Hierarchical-Hybrid 3D Gaussian Splatting for Compressed Scene Modeling. *arXiv preprint arXiv:2406.08759*.

Zhang, R.; Isola, P.; Efros, A. A.; Shechtman, E.; and Wang, O. 2018. The unreasonable effectiveness of deep features as a perceptual metric. In *Proceedings of the IEEE conference on computer vision and pattern recognition*, 586–595.

A Implementation details

A.1 Latent Feature Field

For hash-based grid features, we have chosen 16 levels of grid resolutions, with each level’s hash table having a length of 2^{19} and a 2-dimensional feature vector. To model high-dynamic-range scenes, we employ third-order spherical harmonics encoding for directions. Additionally, we utilize a two-layer lightweight MLP to compress the concatenated view-independent features and directional encodings, resulting in a 16-dimensional feature map.

A.2 Image Decoder

To compensate for the information loss caused by grid feature interpolation, we utilize a lightweight image decoder to decode the feature map rendered by the MFGS pipeline. For the architecture of this decoder, we have chosen Bottleneck (He et al. 2016) as the backbone to ensure computational efficiency. It is configured with a single layer, with a maximum feature dimension of 256, as detailed in Figure 8. Additionally, we employ convolution to upscale the feature map from 16 to 256 dimensions and to downscale the output of the bottleneck from 256 to 3 dimensions. The upscaling uses a 3×3 convolution kernel, while the downscaling employs a 1×1 convolution kernel.

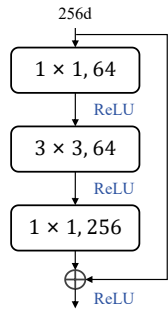


Figure 8: Architecture of Bottleneck.

A.3 Additional Details

We report different metrics from the original SRGS (Feng et al. 2024) paper, primarily due to differences in resolution settings and scene selection. For the Tanks&Temples dataset, we only choose 2 scenes (Train and Truck) following the 3DGS (Kerbl et al. 2023) approach, whereas SRGS selects 4 scenes. Additionally, our choice of SwinIR (Liang et al. 2021) architecture may differ. In this paper, we opt for a middle-sized SwinIR pretrained on the DIV2K (Agustsson and Timofte 2017), Flickr2K (Lim et al. 2017), and OST (Wang et al. 2018) datasets for all baselines and our method. For the ground truth high-resolution images, we employ bilinear interpolation for downsampling, while SRGS uses bicubic interpolation. This difference in approach can still lead to variations in results.

B Addtional Results

B.1 Robustness of MFGS

We further test MFGS on the HRNVS task without using any 2D prior, where we train with low-resolution scenes and directly render high-resolution images. Compared to 3DGS (Kerbl et al. 2023) and Scaffold-GS (Lu et al. 2024), MFGS demonstrates superior visual effects. Figure 9 provides a comparative analysis of the rendering results, showcasing the robustness of MFGS for the HRNVS task.

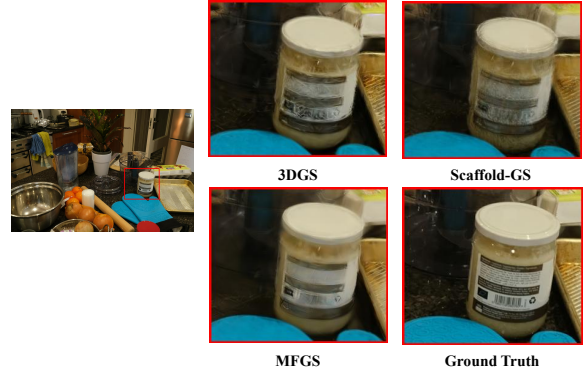


Figure 9: Qualitative comparison of MFGS with 3DGS and Scaffold-GS for HRNVS ($\times 4$) without a 2D prior, demonstrating the robustness of MFGS across various resolutions.

B.2 More comparison with SRGS

We test the scenario where some high-resolution ground truth input views are used as supervision and compare the performance of our method with SRGS under different proportions of true and pseudo labels, as shown in Figure 10. Our method consistently outperforms SRGS in all situations. Moreover, even without true high-resolution images, our method performs better than SRGS with 20% true high-resolution images.

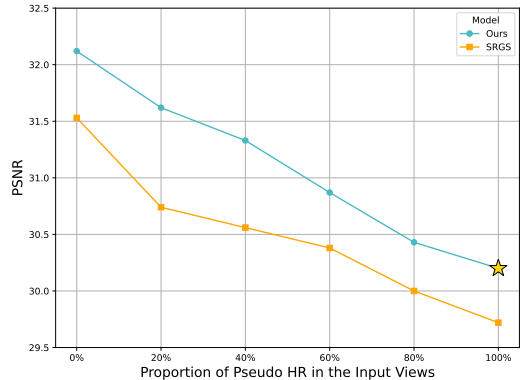


Figure 10: Comparison of our method and SRGS using a mix of ground truth HR and pseudo HR for supervision on the room scene from Mip-NeRF360 Dataset for HRNVS($\times 4$).

B.3 Per-scene Results

We provide additional quantitative results over all real-world scenes, as shown in Table 5-13.

B.4 More qualitative evaluation

We present additional qualitative comparisons in Figure 11.

Table 5: PSNR scores for Real-world Datasets on NVS ($\times 1$) task.

Dataset Methods&Scenes	room	kitchen	bonsai	Mip-NeRF360						Tanks&Temples drjohnson	Deep Blending train	Deep Blending truck	
				counter	bicycle	flowers	garden	stump	treehill				
3DGS	32.75	32.99	32.69	29.36	26.80	21.57	27.37	26.67	22.56	28.43	29.06	22.67	26.55
Scaffold-GS	33.52	34.07	34.44	30.87	26.82	23.15	29.60	27.16	24.33	29.69	29.68	23.81	27.52
Ours	34.30	34.29	34.84	30.58	27.03	23.05	29.72	26.90	24.28	29.39	30.36	24.81	27.89

Table 6: SSIM scores for Real-world Datasets on NVS ($\times 1$) task.

Dataset Methods&Scenes	room	kitchen	bonsai	Mip-NeRF360						Tanks&Temples drjohnson	Deep Blending train	Deep Blending truck	
				counter	bicycle	flowers	garden	stump	treehill				
3DGS	0.959	0.966	0.956	0.921	0.843	0.606	0.867	0.772	0.634	0.871	0.877	0.855	0.910
Scaffold-GS	0.965	0.969	0.971	0.944	0.840	0.709	0.921	0.810	0.726	0.898	0.896	0.875	0.919
Ours	0.963	0.969	0.969	0.935	0.834	0.691	0.915	0.799	0.718	0.892	0.904	0.880	0.920

Table 7: LPIPS scores for Real-world Datasets on NVS ($\times 1$) task.

Dataset Methods&Scenes	room	kitchen	bonsai	Mip-NeRF360						Tanks&Temples drjohnson	Deep Blending train	Deep Blending truck	
				counter	bicycle	flowers	garden	stump	treehill				
3DGS	0.059	0.034	0.097	0.113	0.127	0.336	0.107	0.215	0.326	0.138	0.120	0.127	0.079
Scaffold-GS	0.047	0.032	0.039	0.059	0.133	0.023	0.060	0.164	0.222	0.112	0.101	0.110	0.072
Ours	0.061	0.034	0.048	0.075	0.163	0.265	0.074	0.184	0.264	0.119	0.100	0.120	0.078

Table 8: PSNR scores for Real-world Datasets on HRNVS ($\times 2$) task.

Dataset Methods&Scenes	room	kitchen	bonsai	Mip-NeRF360						Tanks&Temples drjohnson	Deep Blending train	Deep Blending truck	
				counter	bicycle	flowers	garden	stump	treehill				
3DGS	28.37	23.35	25.75	25.66	21.63	19.73	22.11	23.11	21.01	27.57	28.18	20.65	20.91
3DGS-SwinIR	29.34	24.80	27.29	26.93	23.24	20.50	24.16	24.92	21.73	27.35	27.77	20.60	23.62
Scaffold-GS	27.92	23.82	24.73	25.67	21.76	19.78	21.74	23.18	21.75	28.32	29.25	21.19	20.60
Scaffold-SwinIR	29.90	24.84	27.76	27.52	23.00	19.79	24.09	23.57	22.03	27.93	28.24	20.98	23.95
SRGS	30.27	27.80	31.00	27.60	24.45	21.53	25.86	25.62	22.05	28.43	29.53	22.16	24.40
Ours	31.62	28.41	32.04	28.52	24.43	21.21	26.04	25.36	22.57	29.05	30.17	23.55	25.27

Table 9: SSIM scores for Real-world Datasets on HRNVS ($\times 2$) task.

Dataset Methods&Scenes	room	kitchen	bonsai	Mip-NeRF360						Tanks&Temples drjohnson	Deep Blending train	Deep Blending truck	
				counter	bicycle	flowers	garden	stump	treehill				
3DGS	0.888	0.840	0.865	0.833	0.652	0.525	0.714	0.666	0.558	0.857	0.868	0.750	0.786
3DGS-SwinIR	0.872	0.746	0.843	0.826	0.631	0.529	0.681	0.688	0.553	0.843	0.848	0.715	0.814
Scaffold-GS	0.891	0.843	0.854	0.841	0.633	0.516	0.702	0.660	0.567	0.880	0.890	0.771	0.792
Scaffold-SwinIR	0.878	0.747	0.845	0.834	0.621	0.507	0.679	0.669	0.550	0.855	0.854	0.724	0.822
SRGS	0.904	0.846	0.925	0.866	0.701	0.589	0.773	0.717	0.592	0.876	0.894	0.793	0.839
Ours	0.909	0.854	0.927	0.872	0.691	0.567	0.765	0.708	0.597	0.879	0.898	0.799	0.844

Table 10: LPIPS scores for Real-world Datasets on HRNVS ($\times 2$) task.

Dataset Methods&Scenes	Mip-NeRF360									Tanks&Temples		Deep Blending	
	room	kitchen	bonsai	counter	bicycle	flowers	garden	stump	treehill	drjohnson	playroom	train	truck
3DGS	0.173	0.161	0.175	0.178	0.288	0.383	0.234	0.306	0.386	0.186	0.162	0.221	0.175
3DGS-SwinIR	0.166	0.214	0.176	0.174	0.266	0.354	0.230	0.272	0.337	0.191	0.174	0.225	0.164
Scaffold-GS	0.161	0.154	0.180	0.174	0.309	0.383	0.233	0.329	0.380	0.152	0.140	0.192	0.161
Scaffold-SwinIR	0.158	0.213	0.172	0.168	0.276	0.351	0.231	0.288	0.330	0.166	0.163	0.213	0.157
SRGS	0.171	0.171	0.139	0.163	0.261	0.349	0.201	0.269	0.363	0.170	0.148	0.198	0.153
Ours	0.174	0.167	0.141	0.171	0.296	0.361	0.230	0.290	0.382	0.173	0.153	0.105	0.173

Table 11: PSNR scores for Real-world Datasets on HRNVS ($\times 4$) task.

Dataset Methods&Scenes	Mip-NeRF360									Tanks&Temples		Deep Blending	
	room	kitchen	bonsai	counter	bicycle	flowers	garden	stump	treehill	drjohnson	playroom	train	truck
3DGS	26.03	19.68	22.74	23.21	18.52	16.67	18.17	19.31	19.10	24.65	24.94	18.51	17.22
3DGS-SwinIR	28.39	23.75	26.14	26.02	21.63	19.21	21.96	22.71	21.44	25.63	25.67	19.49	21.64
Scaffold-GS	25.03	20.71	21.79	23.02	18.57	16.70	17.81	19.31	19.72	26.92	28.10	18.50	16.97
Scaffold-SwinIR	28.72	23.76	26.50	26.52	21.45	18.61	21.97	22.25	21.60	27.20	27.70	19.78	21.85
SRGS	29.72	24.86	27.17	26.96	23.23	20.83	25.63	25.85	22.21	28.28	29.32	20.96	22.26
Ours	30.20	26.10	27.84	27.44	23.72	20.69	25.93	25.47	22.57	28.68	29.73	21.81	22.88

Table 12: SSIM scores for Real-world Datasets on HRNVS ($\times 4$) task.

Dataset Methods&Scenes	Mip-NeRF360									Tanks&Temples		Deep Blending	
	room	kitchen	bonsai	counter	bicycle	flowers	garden	stump	treehill	drjohnson	playroom	train	truck
3DGS	0.820	0.688	0.760	0.750	0.458	0.364	0.478	0.472	0.449	0.755	0.783	0.621	0.621
3DGS-SwinIR	0.817	0.672	0.773	0.790	0.474	0.415	0.492	0.538	0.475	0.776	0.801	0.616	0.696
Scaffold-GS	0.817	0.703	0.755	0.762	0.452	0.359	0.461	0.486	0.463	0.854	0.870	0.630	0.627
Scaffold-SwinIR	0.821	0.672	0.776	0.794	0.468	0.394	0.491	0.514	0.468	0.830	0.846	0.619	0.701
SRGS	0.867	0.711	0.826	0.831	0.610	0.535	0.726	0.712	0.569	0.867	0.882	0.695	0.722
Ours	0.856	0.756	0.823	0.830	0.629	0.531	0.731	0.694	0.596	0.869	0.890	0.690	0.725

Table 13: LPIPS scores for Real-world Datasets on HRNVS ($\times 4$) task.

Dataset Methods&Scenes	Mip-NeRF360									Tanks&Temples		Deep Blending	
	room	kitchen	bonsai	counter	bicycle	flowers	garden	stump	treehill	drjohnson	playroom	train	truck
3DGS	0.327	0.338	0.363	0.332	0.442	0.489	0.423	0.456	0.502	0.297	0.273	0.370	0.371
3DGS-SwinIR	0.273	0.319	0.295	0.278	0.372	0.433	0.362	0.376	0.411	0.265	0.250	0.323	0.307
Scaffold-GS	0.318	0.326	0.365	0.329	0.456	0.486	0.424	0.464	0.488	0.302	0.305	0.356	0.355
Scaffold-SwinIR	0.268	0.317	0.292	0.274	0.375	0.424	0.362	0.390	0.399	0.261	0.246	0.311	0.299
SRGS	0.292	0.303	0.292	0.278	0.350	0.403	0.262	0.305	0.418	0.297	0.303	0.323	0.335
Ours	0.298	0.304	0.292	0.288	0.341	0.396	0.263	0.325	0.382	0.308	0.165	0.346	0.358

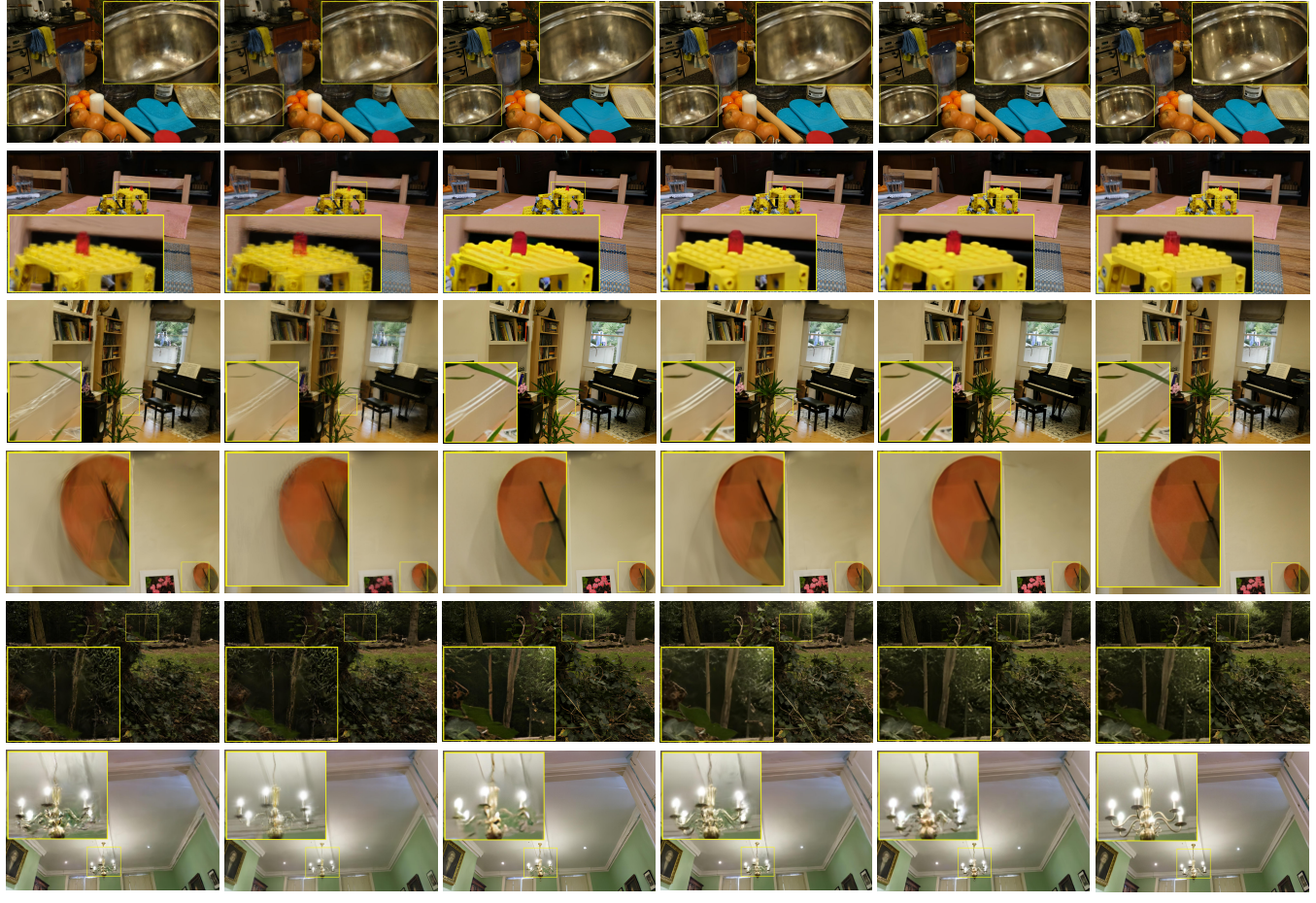


Figure 11: Qualitative comparison of the HRNVS ($\times 4$) on real-world datasets. We highlight the difference with colored patches.